

Determinations of angular stiffness in rotational optical tweezers

Mark L. Watson,^{1,2,*} Alexander B. Stilgoe,^{1,2} and Halina Rubinsztein-Dunlop^{1,2}

¹*School of Mathematics and Physics, The University of Queensland, St Lucia, Brisbane, 4072, Queensland, Australia*
²*ARC CoE in Quantum Biotechnology, The University of Queensland, St Lucia, Brisbane, 4072, Queensland, Australia*

(Dated: December 9, 2025)

Rotational optical tweezers are used to probe the mechanical properties of unknown microsystems. Quantifying the angular trap stiffness is essential for interpreting the rotational dynamics of probe particles. While methods for trap stiffness calibration are well established for translational degrees of freedom, angular trapping has been largely overlooked and is often assumed to behave analogously to translational dynamics. However, rotational and translational motions are sensitive to distinct experimental parameters and offer separate insights. This work covers passive analysis techniques for calibrating the angular trap stiffness and examines the influence of several factors unique to rotational optical tweezers. We show that the parameters of an ancillary measurement beam can be tuned to minimise its influence on angular trapping dynamics, while offering unprecedented improvements for nanoparticle analysis. We also explore the combined effects of shape-induced and material birefringence in spheroidal vaterite probes, and present a framework for assessing hydrodynamic and inertial contributions. These results provide a foundation for characterising rotational optical tweezers independent from translational models.

I. INTRODUCTION

Optical tweezers (OTs) is a powerful experimental tool widely employed to investigate both fundamental and applied phenomena at micro-to-nanoscopic size scales [1–3]. Their success stems from the ability to trap microscopic particles and perform precise measurements of position, angle, force, and torque. When OTs are used to extract physical properties of local microenvironments, it is necessary to use a well-characterised probe particle and accurately establish its interaction with the optical potential. Analysis of the probe’s dynamics can be interpreted to accurately attribute the results to the desired phenomena. This is particularly useful in microrheology studies of biological systems [4–7] and quantifying microscopic forces and torques [8–14].

In most trapping experiments, the optical potential that confines the particle in space is treated as harmonic for small displacements from the equilibrium position, \mathbf{x}_0 . In this regime, the force is proportional to displacements, such that $\mathbf{F}_{\text{opt}}(t) = -\boldsymbol{\kappa}(\mathbf{x}(t) - \mathbf{x}_0)$ where $\boldsymbol{\kappa} = (\kappa_x, \kappa_y, \kappa_z)$ is the translational trap stiffness about each axis. Determining $\boldsymbol{\kappa}$ is an important starting point for quantitative optical tweezers measurements and forms a substantial portion of optical tweezers literature, appearing in reviews of established techniques and as a vital detail in the experimental methodology attached to research articles [15–17]. Consequently, calibrations have become routine, often favouring the equipartition analysis for a simple estimate of trap stiffness or power spectrum analysis for a more robust and reliable estimate [15, 16].

Rotational measurements with optical tweezers are interested in either the rotation or alignment dynamics of

the probes [6, 18–24]. In the context of alignment, the optical torque creates an angular confining potential that can be quantified by its angular trap stiffness, χ . Rotational measurements are less common with comparatively less published work that addresses characterising the interaction between the angular dynamics of the probe with the optical potential for applications. However, determining χ is of vital importance for wideband rotational microrheometry and for rotational ballistic measurements [24, 25].

Calibrations in rotational optical tweezers have previously focussed on accurate torque detection, [26], or assume that the angular dynamics are exactly analogous to the translational dynamics, so similar approaches can be employed. However, there are significant differences between rotational and translational tweezers experiments and descriptions of the probe dynamics are not strictly interchangeable. The two regimes have different sensitivities for experimental parameters and offer separate insights into systems. For example, translational and rotational hydrodynamics effects differ vastly, which is particularly important in the context of biofluids and biological microsystems that are inherently inhomogeneous [27–30].

This work aims to provide a framework for angular trap stiffness calibration about the beam axis. The results presented here are based on a typical rotational optical tweezers system with vaterite microspheres as birefringent probe particles. The mechanism underpinning this system is detailed in Section II, which describes the apparatus, the expected dynamics of the vaterite probe, and the detection method. Whilst our results focus on this specific configuration, the methodology can be extended to other rotational probes and experimental parameters.

The results are presented across three distinct sections. Section III introduces several analysis techniques that are applied to experimental data to demonstrate the straightforward calibration procedure for determining angular

* mark.watson@uq.edu.au

stiffness. Section IV adopts a computational approach, calculating the angular trap stiffness directly from the simulated torque profile. This method allows system parameters to be varied to explore the resulting dynamics. Finally, Section V examines, through computational methods, several factors that influence angular trap stiffness and are unique to rotational optical trapping. These include the contribution from a measurement beam, hydrodynamic and inertial effects, and probe morphology. Overall, this study provides a systematic methodology for determining the angular trap stiffness and highlights the unique consequences for the rotational regime.

II. METHODOLOGY

A. Rotational optical tweezers (ROTs) system

Rotational optical tweezers (ROTs) exploits the conservation of linear momentum for optical trapping while also introducing rotation by considering the total angular momentum of the system. Photons can carry spin angular momentum of $\pm\hbar/\text{photon}$, as well as orbital angular momentum from the spatial distribution of their wavefront. As the light interacts with a particle, a transfer of angular momentum can occur, producing an optical torque and a change to the total angular momentum flux of the light. Rotational optical tweezers offer highly flexible control over particle dynamics, with tunable beam shape and polarisation enabling precise manipulation of torque, alignment, and rotational confinement. However, we restrict our discussion to the transfer of spin angular momentum to a birefringent probe. Fig. 1 shows the rotational optical trapping system used to achieve the desired dynamics.

The optical trap is formed using a 1064 nm Nd:YAG laser focussed by a high numerical aperture objective lens (Olympus UPLSAPO60XW, 60 \times , 1.2 NA, water). The optical power is controlled using an acousto-optic modulator (AOM, DTD-274HD6 driven at 27 MHz). The forward transmitted light is collected by a high NA condenser lens (Olympus U-AA, 1.4 NA, oil). D_{0-3} are photovoltaic detectors (PDA36A-EC, Thorlabs) used to measure the initial power of the beams (D_0 for IR, D_3 for He-Ne) and the power of right (D_1) and left (D_2) circular polarisation components. Half waveplates ($\lambda/2$) and quarter waveplates ($\lambda/4$) are used to control the polarisation state of the trap and the polarisation basis of the detection schemes.

Precise measurements of optical torque and angular position are performed using sensitive polarisation detection. The optical torque is determined by measuring the spin angular momentum per photon, σ , such that

$$T_{\text{opt}} = \Delta\sigma P/\omega, \quad (1)$$

where P is the power of the trapping beam, ω is the angular frequency of the trapping light, and $\Delta\sigma = \sigma_{\text{in}} - \sigma_{\text{out}}$.

Here, σ is equivalent to the degree of circular polarisation of the light. σ is measured by detecting the proportion of right and left circularly polarised light from

$$\sigma_{\text{out}} = (D_1 - D_2)/(D_1 + D_2). \quad (2)$$

The trap power is proportional to the intensity of the incident beam, such that $P = \varepsilon D_0$ where ε is a calibration constant converting the detector voltage to optical power. Importantly, the system incorporates a removable quarter-wave plate before the trap, enabling straightforward switching between linear and circular polarisation states.

The optical torque acting on the probe—in our case, a vaterite microsphere—depends on its anisotropy and inhomogeneity. Vaterite microspheres are widely used for rotation experiments, due to their spherical geometry, strong birefringence, and routine synthesis protocol [31]. Vaterites are positive uniaxial crystals that—given certain conditions—can undergo spherulite growth where the extraordinary axis of individual crystal follows a rotationally symmetric hyperbolic distribution [31]. An optic axis, defined parallel to this symmetry axis, is used to describe the orientation of the probe. Since the torque detection detects torque about the beam axis, only the azimuthal trajectory, ϕ , is measured.

The angular position of the probe is detected using an independent measurement beam, in this case a 633 nm Helium-Neon laser ((He-Ne), HL210LB, Thorlabs) that is weakly focussed and operated at significantly lower power to minimise any contribution to the optical trap (see Section V A). The beam is initially circularly polarised, and the angular position is determined by measuring the change in polarisation in a linear polarisation basis. The probe acts as a partial waveplate with a fast axis defined by its optic axis. As ϕ varies, the proportion of power between polarisation components in a fixed linear basis changes sinusoidally. Hence, the detection is based on

$$\sin(2\phi) \propto (D_4 - D_5)/(D_4 + D_5), \quad (3)$$

where the factor of 2 accounts for the probe's mirror symmetry. D_4 and D_5 are the voltage signals. A half waveplate is positioned before the polarisation beam splitter cube, so when at the equilibrium orientation the angular sensitivity is maximised. We have incorporated a balanced photodetector (HBPR-100M-60K-SI, Femto) to measure the equivalent of $D_4 - D_5$ with the common mode noise filtered out. This is necessary when optimising the angular sensitivity, as in the case of rotational ballistic measurements, [24]. For this work, where that level of sensitivity was not required, we restricted the angular measurement to the separate signals from D_4 and D_5 .

In a circularly polarised trap, there is a continuous transfer of spin-angular momentum that generates an optical torque independent of its azimuthal orientation. In this configuration, the microsphere rapidly reaches terminal angular velocity, determined by the balance between

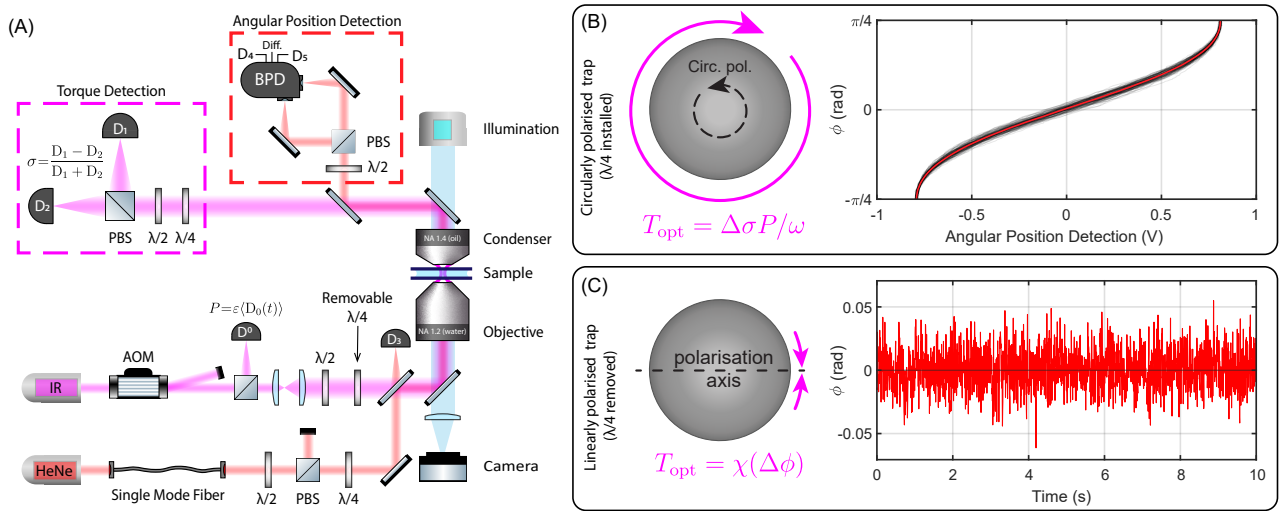


Figure 1. (A) Simplified schematic of the rotational optical tweezers system. (B) Circular polarisation configuration used to calibrate for angular displacement. The plot shows the conversion from volts to radians, where the black traces are segments taken from the time trace of the rotating vaterite and the red line is the mean. (C) Linear polarisation configuration and the measurement of the probe's azimuthal trajectory are used for angular trap-stiffness calibration.

the optical torque and viscous drag. The latter is given by $T_{\text{drag}} = 8\pi\eta a^3\Omega$, where η is the viscosity, a the radius, and Ω the rotation rate. Measurements of the constant rotation are used to calibrate Eq. 3, as the entire voltage readout is sampled. The plot in Fig. 1B shows the conversion from the voltage signal to radians. The recorded voltage varies sinusoidal to twice the azimuthal angle of the vaterite, $V \propto \sin(2\theta)$ [23]. Fig. 1B overlays segments of the detected voltage from a rotating vaterite and converts these to azimuthal angle, ϕ , in radians. The black traces have been segments between maxima and minima and the red line shows the mean result. This plot demonstrates that slight variation in trajectory as the particle rotates.

When trapped in linearly polarised light, the probe aligns with the polarisation axis of the incident beam and orthogonal to the propagation direction, producing an equilibrium orientation ϕ_0 . Thermal motion results in fluctuations of angular position around the equilibrium. With the angle calibration determined from the probe rotating, the angular trajectory is obtained, allowing for the determination of the angular stiffness or for analysis of angular dynamics used to probe a system of interest. An example trajectory of a probe in this configuration is shown in Fig. 1C. The optical torque about the beam axis is given by $T_{\text{opt}}(t) = (\chi/2)\sin(2(\phi(t) - \phi_0))$ which for small angles can be treated as $T_{\text{opt}}(t) = -\chi(\phi(t) - \phi_0)$. This provides a second method to determine the optical torque using the measurement beam, given χ is known, that matches the polarisation-based torque detection from the trapping beam.

There are two other rotational degrees of freedom that should be considered, suggesting an angular trap stiffness vector of $\chi = (\chi_\rho, \chi_\theta, \chi_\phi)$. The first is the roll of the vaterite, which is its rotation about its optic axis. Due to

the rotational symmetry, there is no optical torque generated about this axis so $\chi_\rho = 0$. The second is the elevation of the vaterite, which is the out-of-plane rotation from the plane orthogonal to the beam propagation direction. Since the optic axis remains in this plane regardless of incident polarisation, there is an associated angular stiffness, χ_θ . This degree of freedom is difficult to measure precisely, particularly with vaterite, but has been investigated using other rotational probes [32, 33]. As mentioned earlier, we restrict our analysis to the azimuthal stiffness, χ_ϕ .

The experiment results presented here are for a 1.5 μm radius probe. Time series data was collected at 20 kHz for 20 s. This allowed sufficient time for segmenting the data and obtaining strong time-averaging. The experimental system is controlled using custom software written in LabVIEW. The resulting data was analysed using MATLAB2024b.

B. Computational methods

The computational results presented in this paper use the Optical Tweezers Toolbox [34] to calculate the interaction between the probe and the light, via the T-matrix method for scattering calculations [35]. Briefly, this involves modelling the electric field of this incident and scattered light as a series expansion of vector spherical wave functions (VSWF), with expansion coefficients \mathbf{a} and \mathbf{p} respectively. The T-matrix describes the coupling between \mathbf{a} and \mathbf{p} in the presence of a scatterer, such that $\mathbf{p} = \mathbf{T}\mathbf{a}$, allowing calculation of the scattered field for calculations of force and torque [35, 36]. The T-matrix is independent of the incident field, enabling repeated calculations in a particle-centred coordinate system, making

it ideal for investigating the force and torques at arbitrary positions and orientations. The T-matrix that represents the scattering of vaterite microspheres was formulated using the discrete dipole approximation with point matching [37]. The volume of the probe is discretised into an array of closely spaced dipoles ($< \lambda/20$ typical spacing), with the polarisability of each dipole defined, accounting for the material anisotropy and inhomogeneity, following the internal structure described by Loke *et al.* [37].

III. DETERMINATION OF STIFFNESS FROM ANGULAR TRAJECTORIES

Determination of trap stiffness from stochastic trajectories requires an accurate model of the underlying dynamics. For this case, that is a model describing the azimuthal trajectory of the probe when trapped by linearly polarised light. For clarity, we take $\phi(t)$ as the angular displacement from equilibrium (i.e. choose $\phi_0 = 0$). We assume the azimuthal trajectory is independent of other degrees of freedom, and restrict the following analysis to 1D rotational dynamics motion without any coupling.

The equation of motion follows the Einstein-Ornstein-Uhlenbeck theory of rotational Brownian motion, written as the Langevin equation [23],

$$I\ddot{\phi}(t) + \gamma_0\dot{\phi}(t) + \chi\phi(t) = \sqrt{2k_B T \gamma_0} \xi(t), \quad (4)$$

where $I = (2/5)ma^2$ is the inertia of the probe (mass m , radius a), $\gamma_0 = 8\pi\eta a^3$ is the Stokes rotational drag coefficient for a sphere in a viscous medium, k_B is Boltzmann's constant, T is the temperature, and $\xi(t)$ is a Gaussian white-noise term with $\langle \xi(t) \rangle = 0$, $\langle \xi(t)^2 \rangle = 1$, and $\langle \xi(t)\xi(t') \rangle = \delta(t - t')$.

The right hand side of Eq. 4 represents the rotational Brownian motion that drives angular fluctuations about equilibrium. The rate at which the angular trajectory returns to the equilibrium is set by the characteristic trap time, $\tau_{\text{opt}} = \gamma_0/\chi$, which is the ratio of the drag coefficient to the angular trap stiffness. Hence, the calibration techniques often analyse the temporal or frequency correlations of the angular trajectory to determine τ_{opt} as an intermediate step before obtaining χ .

Typically, the inertia dissipation occurs significantly faster than the experimental measurement rate (on the order of 10^{-6} s), such that $I\ddot{\phi}(t) \simeq 0$. The angular trajectory can be approximated as

$$\dot{\phi}(t) + \frac{\phi(t)}{\tau_{\text{opt}}} = \sqrt{2D} \xi(t), \quad (5)$$

where $D = k_B T / \gamma_0$ is the rotational diffusion constant. The formal solution of this Langevin equation, in the domain $[0, t]$, is given by

$$\phi(t) = \phi(0)e^{-t/\tau_{\text{opt}}} + \sqrt{2D} \int_0^t \xi(s) e^{-(t-s)/\tau_{\text{opt}}} ds. \quad (6)$$

To extract the angular trap stiffness from experimental trajectories, we employ several complementary analysis techniques that exploit different statistical properties of the angular fluctuations and are frequently used in the calibration of translational trap stiffness. These include equipartition (EQP), mean-squared displacement (MSD), autocorrelation function (ACF), power spectral density (PSD), and maximum likelihood estimation (MLE) methods. Each provides a complementary route to determine χ , with distinct advantages and sensitivities to experimental artefacts such as finite sampling, calibration accuracy, or detector noise. By applying all five approaches to the same dataset, we both validate the consistency of the extracted stiffness and highlight the practical considerations that arise in their implementation.

A. Equipartition (EQP) Analysis

The simplest approach to determine the angular trap stiffness is through the equipartition theorem, which relates the thermal energy of the system to the variance of the angular fluctuations on timescales much larger than the characteristic trapping time. In the harmonic approximation, this becomes

$$\frac{1}{2}\chi\langle\phi(t)^2\rangle = \frac{1}{2}k_B T. \quad (7)$$

A direct expression of χ can be obtained as

$$\chi = \frac{k_B T}{\langle\phi(t)^2\rangle}. \quad (8)$$

In practice, $\langle\phi(t)^2\rangle$ is obtained from the experimentally measured angular trajectory after subtracting any slow drift or offset. This method is straightforward and requires only a measurement of angular position, with no knowledge of the local viscosity, making it attractive for rapid estimation of χ . Its accuracy critically depends on the precision of the angular calibration, and the validity of the approach relies on the assumption that the probe remains in the linear regime of the trap, and that a sufficiently long measurement time to adequately sample the distribution has been made. The histograms in Fig. 2A show the count of angular position for a probe at three different trapping powers. Higher trapping powers lead to stiffer traps, resulting in a smaller variance. Fig. 2B presented the same data on a logarithmic scale, fitted with a quadratic function to obtain χ . Only the central 99% of the data was used, as the counts at larger angular displacements were insufficient for a reliable average.

B. Mean-squared displacement (MSD) Analysis

The mean-squared displacement of the angular trajectory offers an alternative approach to determine χ . The

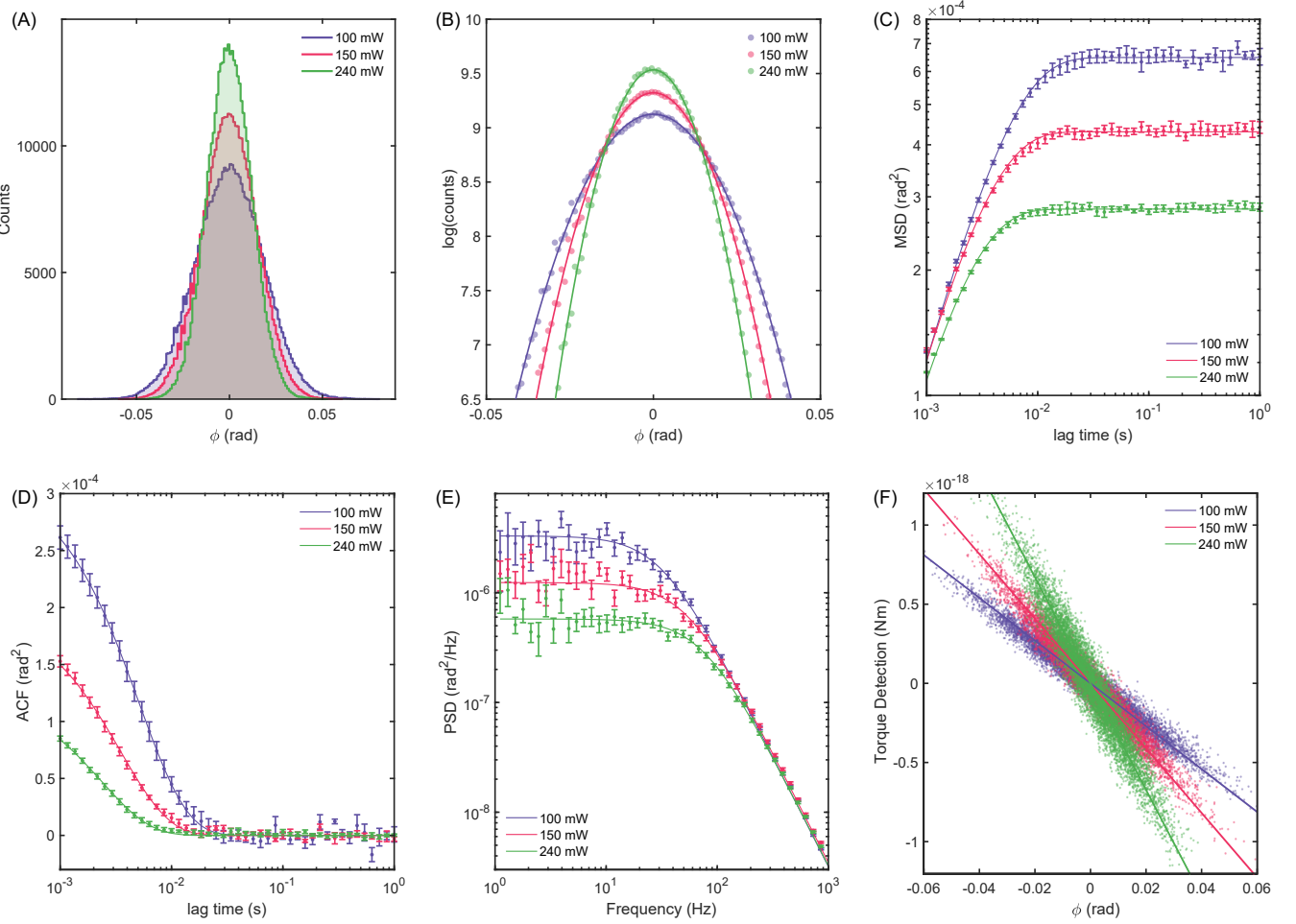


Figure 2. (A) Histogram of detections. (B) $\log(\text{counts})$ histogram with quadratic fit to demonstrate harmonic potential. Fitting 99% of centred data. Experimental results of (C) MSD, (D) ACF, (E) PSD for a $1.5\text{ }\mu\text{m}$ radius vaterite trapped at varying powers fitted by the expected model. (F) The linear relationship between optical torque and angle where overlaid lines have a gradient calculated using the MLE method.

MSD of a particle, $\langle(\phi(t + \tau) - \phi(t))^2\rangle$, quantifies the average displacement a particle can travel given some lag time, τ . A free particle undergoing rotational diffusion has an $\text{MSD} \propto \tau$. The angular confinement from the optical trap prevents the particle from freely diffusing and introduces an exponential decay to the MSD, which plateaus at time scales longer than τ_{opt} .

The theoretical MSD can be derived using Eq. 6 as follows:

$$\text{MSD}(\tau) = \langle(\phi(t + \tau) - \phi(t))^2\rangle, \quad (9)$$

$$= \langle\phi(t + \tau)^2\rangle - 2\langle\phi(t + \tau)\phi(t)\rangle + \langle\phi(t)^2\rangle, \quad (10)$$

From the equipartition theorem, we know that $\langle\phi(t)^2\rangle = \langle\phi(t + \tau)^2\rangle = k_B T / \chi$. The remaining term in Eq. 10 is the correlation between two lag times. Starting with the

generalised time-domain solution in Eq. 6, this becomes

$$C_\phi(\tau) = \langle\phi(t + \tau)\phi(t)\rangle \quad (11)$$

$$= \langle\phi(t)^2\rangle e^{-\tau/\tau_{\text{opt}}} + \sqrt{2D} \cdot \left\langle \phi(t) \int_t^{t+\tau} \xi(s) e^{-(t+\tau-s)/\tau_{\text{opt}}} ds \right\rangle, \quad (12)$$

$$= \frac{k_B T}{\chi} e^{-\tau/\tau_{\text{opt}}}, \quad (13)$$

where the integral for $s \in [t, t + \tau]$ vanishes because the noise term, $\xi(s)$, is independent of $\phi(t)$ in this domain and has a mean of zero. Therefore, the expected MSD becomes

$$\text{MSD}(\tau) = \frac{2k_B T}{\chi} \left(1 - e^{-\tau/\tau_{\text{opt}}}\right). \quad (14)$$

To explore the behaviour of the MSD, we can take a first-

order series expansion at short and long time scales:

$$\text{MSD}_{\tau \ll \tau_{\text{opt}}}(\tau) \approx \frac{2k_B T}{\gamma_0} |\tau| = 2D|\tau|, \quad (15)$$

$$\text{MSD}_{\tau \gg \tau_{\text{opt}}}(\tau) \approx \frac{2k_B T}{\chi} = 2D\tau_{\text{opt}}. \quad (16)$$

As expected, $\text{MSD}_{\tau \ll \tau_{\text{opt}}} \propto \tau$ corresponding to free rotational diffusing, while $\text{MSD}_{\tau \gg \tau_{\text{opt}}}$ is the the maximum displacement reached by the particle.

Fig. 2C shows the experimental MSD calculated at specific lag times obtained for three different trapping powers, together with fits to the theoretical form (Eq. 14). Increasing trap power leads to a faster saturation and a lower plateau, consistent with a stiffer angular potential. Fitting the experimental MSD data to the theoretical expression yields both τ_{opt} and χ , allowing a simultaneous estimation of γ_0 and stiffness.

This method is robust to slow drift and does not require explicit calibration of the torque signal. However, it is sensitive to finite trajectory length and sampling rate, which can bias the long-lag plateau. When calculating the MSD, either overlapping (evaluating the displacement for every possible time origin) or non-overlapping intervals can be used. The overlapping approach provides a much larger number of data points for averaging, allowing the MSD curve to be resolved with shorter measurement times. However, successive MSD values are not strictly independent introducing correlations between points. By contrast, non-overlapping calculations avoid this correlation but require substantially longer trajectories to achieve the same statistical precision.

In practice, overlapping MSD estimates are commonly used for their higher resolution, with more conservative error estimates obtained through block averaging. Typically, the full trajectory is segmented into shorter windows, with χ taken as the mean of the estimates from each segment and the uncertainty given by the standard error across segments.

C. Autocorrelation function (ACF) Analysis

The autocorrelation function (ACF) provides a complementary description of the angular dynamics that is linked to the MSD. While the MSD emphasises the growth of angular fluctuations over some lag time, the ACF highlights the decay of correlations back to equilibrium. Angular confinement ensures that positions separated by short time intervals remain correlated. The correlation is given by:

$$C_\phi(\tau) = \langle \phi(t)\phi(t+\tau) \rangle = \frac{k_B T}{\chi} e^{-\tau/\tau_{\text{opt}}}, \quad (17)$$

where the solution follows directly from the corresponding term in the MSD derivation (Eq. 13). In fact, the MSD and ACF quantities are connected through

$\text{MSD}(\tau) = 2(\langle \phi^2 \rangle - C_\phi(\tau))$. For a discrete trajectory, the correlation is estimated as

$$C_\phi(k) = \frac{1}{N-k} \sum_{j=1}^{N-k} \phi_{j+k}\phi_j, \quad (18)$$

where the lag time is $\tau_k = k\Delta t$, which is used to compute the experimental values of the ACF. Fitting the experimental data to the theoretical expression in Eq. 17 yields both the relaxation time and the angular trap stiffness. Compared with the MSD, the ACF often provides a more direct and statistically efficient estimate of τ_{opt} , since it relies on the decay constant rather than the long-lag plateau.

Fig. 2D shows the measured ACFs for three different trapping powers, together with exponential fits to the theoretical form. Increasing trap power leads to a faster decay of correlations, consistent with a stiffer angular potential. This method is less sensitive to slow drift than equipartition and can resolve the relaxation time from shorter trajectories than the MSD. Although, it can be affected by finite sampling, similar to the MSD method.

D. Power Spectral Density (PSD) Analysis

The power spectral density (PSD) provides a frequency-domain description of the thermally driven angular fluctuations. PSD analysis has become one of the most common methods in optical trapping and microrheology, where it is routinely used to extract trap stiffness and hydrodynamic parameters.

It is mathematically related to the autocorrelation function through the Wiener–Kinchin theorem: the PSD is the Fourier transform of the ACF [38]. The PSD emphasises how the variance of the signal is distributed across frequencies, while the ACF highlights the temporal decay of those correlations. Both approaches contain equivalent information, but the PSD is often preferred in practice due to its robustness against drift and its ability to reveal noise characteristics across a wide frequency range. Computationally, the fast Fourier transform (FFT) algorithms make obtaining the PSD inexpensive compared with directly calculating the autocorrelation for an equivalent number of lag times. In many cases, it is more efficient to compute the ACF by taking the inverse Fourier transform of the PSD.

The power spectrum models the expected behaviour of the PSD. The angular position power spectrum (APPS) is defined as $S_\phi(f) = |\tilde{\phi}(f)|^2$, where the tilde represents the unilateral Fourier transform. The Fourier transform of Eq. 5,

$$(-2\pi i \gamma_0 f + \chi) \tilde{\phi}(f) = \sqrt{2k_B T \gamma_0} \tilde{\xi}(t), \quad (19)$$

is used to determine the power spectrum:

$$S_\phi(f) = \frac{D/(2\pi^2)}{f^2 + f_c^2} |\tilde{\xi}(f)|^2, \quad (20)$$

where $f_c = \chi/(2\pi\gamma_0) = 1/(2\pi\tau_{\text{opt}})$ is the corner frequency, with white noise of power, $|\tilde{\xi}(f)|^2 = 1$. The power spectrum takes the form of a Lorentzian, with a flat plateau at low frequencies consistent with harmonic motion in a high loss medium and a f^{-2} proportionality of decay at high frequencies that is characteristic of Brownian walks [15]. The corner frequency is the inverse of the characteristic angular trapping time constant of the probe in the fluid, and it marks the transition between these regimes, providing a direct measure of the trap stiffness. In an experiment, we cannot find the power spectrum, but instead find the PSD, which is obtained with $S_\phi(f) = |\tilde{\phi}(f)|^2/t_{\text{meas}}$, where t_{meas} is the total measurement time.

Fitting the PSD to Eq. 20 often yields both D and f_c from which a robust estimate of γ_0 and χ are obtained. The experimental noise spectrum can be measured and subtracted from the PSD before fitting to improve accuracy. Fig. 2E shows the PSDs for three different trapping powers, together with Lorentzian fits. Increasing trap power shifts the corner frequency to higher values, consistent with a stiffer angular potential. The data sets are truncated at the Nyquist frequency to minimise aliasing. Windowing and segment averaging are commonly used to reduce spectral leakage and improve statistical reliability. Deviations from the expected dynamics due to the hydrodynamic and inertial effects are discussed later in Section VC and can be neglected for most rotational experiments outside the rotational ballistic regime [24].

E. Maximum Likelihood Estimation (MLE)

Maximum likelihood estimation is an alternative approach to determining the angular trap stiffness. MLE has been employed in translational measurements—by analysing the position or force at sequential time points—to calibrate the translational trap stiffness, diffusion constant, and for 3D reconstruction for the optical potential[16, 39, 40]. In contrast, MLE estimation for angular trap stiffness determination can be achieved without any temporal information by combining two separate measurements of optical torque.

When trapped in the linear regime, the optical torque is typically measured from the change in circular polarisation of the trapping beam: $T_{\text{pol}}(t) = \Delta\sigma(t)P(t)/\omega$. An equivalent measurement of optical torque can be inferred from the angular displacement from equilibrium: $T_{\text{ang}}(t) = \chi\phi(t)$. There is noise associated with each detection scheme that are normally distributed and are largely independent from each other—they only share thermal noise from a few shared optical elements and otherwise experience independent technical, electronic, thermal and shot noise. Hence, any measured difference must be normally distributed, such that:

$$T_{\text{pol}} - \chi\phi \sim \mathcal{N}(0, \mu^2), \quad (21)$$

where μ^2 is the variance of a distribution \mathcal{N} , and T_{pol}

and ϕ are arrays containing each measurement with zero mean (i.e $\phi_i = \phi_i - \bar{\phi}$). We can construct a likelihood function,

$$L(\mathbf{T}_{\text{pol}}, \phi; \chi, \mu^2) = \frac{1}{(2\pi\mu^2)^{\frac{N}{2}}} e^{-\frac{1}{2\mu^2} \sum_i^N (T_{\text{pol},i} - \chi\phi_i)^2}, \quad (22)$$

that can be maximised with respect to χ . Taking $\frac{\partial L}{\partial \chi} = 0$, gives a closed form-estimator

$$\chi = \frac{\sum_i^N \phi_i \cdot T_{\text{pol},i}}{\sum_i^N \phi_i^2}, \quad (23)$$

for the angular trap stiffness. Interestingly, this approach can be modified to estimate the conversion factor from detector D_0 in Fig. 1 to the optical trapping power if χ is already known [6].

Fig. 2F shows a scattering plot of the measured torque and angular displacements with slopes calculated using Eq. 23. The fluctuations from the detection scheme, that is $\mathcal{N}(0, \mu^2)$, cause the data points to spread away from the lines.

MLE can also estimate the rotational diffusion constant from the change in azimuthal angle between each time step, $\Delta\phi_i = \phi_{i+1} - \phi_i$. The equation of motion (5) can be discretised as

$$\Delta\phi_i - \omega_c\phi_i = \sqrt{\frac{2D}{\Delta t}}\xi_i, \quad (24)$$

where $\omega_c = \chi/\gamma = 1/\tau_{\text{opt}}$ is the angular corner frequency. Following previous derivations in the translational regime [39, 40], ω_c is estimated using MLE, by

$$\omega_c = \frac{\sum_i^N (\phi_{i+1} - \phi_i)(\phi_i)}{\sum_i^N \phi_i^2}. \quad (25)$$

This provides an alternative approach to determine χ , with knowledge of γ_0 , relying on the temporal correlation between detections rather than the relationship between the different torque measurements. Following determination of ω_c , the rotational diffusion constant can be estimated by

$$D = \frac{\Delta t}{2N} \sum_i^N (\phi_{i+1} + (\omega_c - 1)\phi_i). \quad (26)$$

F. Summary of passive calibration methods

Fig. 2 and Table I present the results from several calibration techniques. Each method reveals an excellent fit between experimental data and theory. The results also demonstrates the effect of increasing trap power on the angular trap stiffness; evidenced by the narrowing distribution of angular displacements (Fig. 2A-B), a shift in the decay constants associated with the characteristic

	100 mW	150 mW	240 mW
EQP	12.6 ± 0.1	18.7 ± 0.2	29.7 ± 0.4
MSD	12.6 ± 0.1	19.0 ± 0.1	29.1 ± 0.1
ACF	12.7 ± 0.1	19.5 ± 0.2	30.2 ± 0.4
PSD	12.7 ± 0.3	19.5 ± 0.6	29.8 ± 0.8
MLE	12.6 ± 0.1	19.0 ± 0.1	30.3 ± 0.2

Table I. Estimates of angular trap stiffness, χ , obtained for a probe at three different trapping powers with units $\text{pN} \mu\text{m rad}^{-1}$ using the corresponding analysis techniques specified by the first column. The uncertainties are taken from the 95% confidence intervals from fitting.

angular trap time (Fig. 2C-E), or the slope between the torque detection and angular displacements (Fig. 2F).

So far, we see that the calibration results from rotational optical tweezers experiments shadow those of regular optical tweezers. However, these similarities end at the assumption of a linear model. The mode of measurement and the differences in how angular momentum is transferred become more important in the following sections.

IV. NUMERICAL DETERMINATION OF STIFFNESS

Having established consistent estimates of the angular trap stiffness from multiple experimental approaches, we will use numerical simulations to investigate how the angular trap stiffness varies from calibrations away from the linear stiffness limit. Computational methods offer two complementary routes to achieve this. Firstly, angular trajectories can be simulated free from instrumental drift, aliasing, and detector noise, allowing us to isolate the intrinsic stochastic dynamics of the trapped probe. These results can serve as a benchmark for the stochastic estimates. Secondly, the angular trap stiffness can be computed directly by calculating the transfer of angular momentum to the probe particle as its angular displacement ϕ is varied. This methodology enables systematic exploration of different trapping configurations and the influence of specific parameters on the angular trap stiffness in controlled systems.

The following numerical results were obtained using the T-matrix method implemented in the Optical Tweezers Toolbox [34] to calculate the optical force and torque on the probe particle [35, 37]. The translational trap stiffness and equilibrium position can be obtained from the force profile, i.e. the force-displacement curve along each axis. Fig. 3A shows the force profiles for a probe of radius 1λ . Owing to the rotational symmetry of the beam, spherical particles often have their equilibrium position (x_0, y_0, z_0) on the beam axis. Consequently, the force profile is first calculated along the z-axis to determine the axial trapping location. The local slope of the force-displacement curve about this equilibrium in the \hat{x} ,

\hat{y} , and \hat{z} directions then defines the corresponding trap stiffnesses, κ_x , κ_y , and κ_z , respectively.

A similar approach can be applied to each rotational degree of freedom, with the torque profiles shown in Fig. 3B. There is an alignment torque in the azimuthal and out-of-plane rotations, which can be used to define χ_ϕ and χ_θ , respectively. Unlike the azimuthal dynamics, there is an alignment torque that keeps the probe's optic axis orthogonal to the beam propagation direction. As Fig. 3B demonstrates, there is no alignment torque about the probe's optic axis due to the rotational symmetry of its anisotropy, hence $\chi_\rho = 0$.

As with the translational trap stiffness, the angular trap stiffness can be obtained from the local slope of the torque profile at equilibrium. The azimuthal torque profiles are shown in Fig. 3C for three probe sizes, with a solid line indicating the local slope used to extract χ_ϕ . The dependence of the angular trap stiffness on probe size is summarised in Fig. 3D. As expected from the scaling of optical torque with particle cross-section, the angular stiffness increases with radius in a given trap.

The numerical results so far have been calculated for a beam focussed by a NA 1.2 water-immersion objective, corresponding to the objective lens in our ROTs system. However, computational results can be used to investigate the angular trap stiffness with a variety of experimental parameters. Fig. 3E maps the influence of probe size and beam convergence angle on the angular trap stiffness. As the convergence angle increases, there is a greater transfer of spin angular momentum due to the larger scattering cross-sections and the shift in the axial equilibrium position toward the beam focus. The optical torque is maximised at the beam focus, so the angular stiffness is sensitive to changes in the axial equilibrium. At low convergence angles a stable trap may not form, which appears as empty regions in the heat map. The boundary of this unstable region oscillates with probe radius due to interference effects [41].

For comparison, Fig. 3F presents a heat map of the optical torque dependent on probe size and beam convergence angle for a probe in a circularly polarised beam. In this case, the optical torque about the beam axis is independent of ϕ , but its magnitude varies systematically with the convergence angle and the axial equilibrium position. The overall trend mirrors that observed for the angular stiffness in linearly polarised traps. Notably, the boundaries of the stable trapping region shift slightly under circular polarisation, reflecting the altered balance between gradient and scattering forces compared with the linearly polarised case.

The numerical results presented in Fig. 3 provide a detailed picture of the optical torque acting on the vaterite probe in a standard optical trapping beam. The force and torque profiles establish the equilibrium positions and stiffnesses, while the scaling with probe size and convergence angles highlights how angular confinement strength can be tuned experimentally. It should

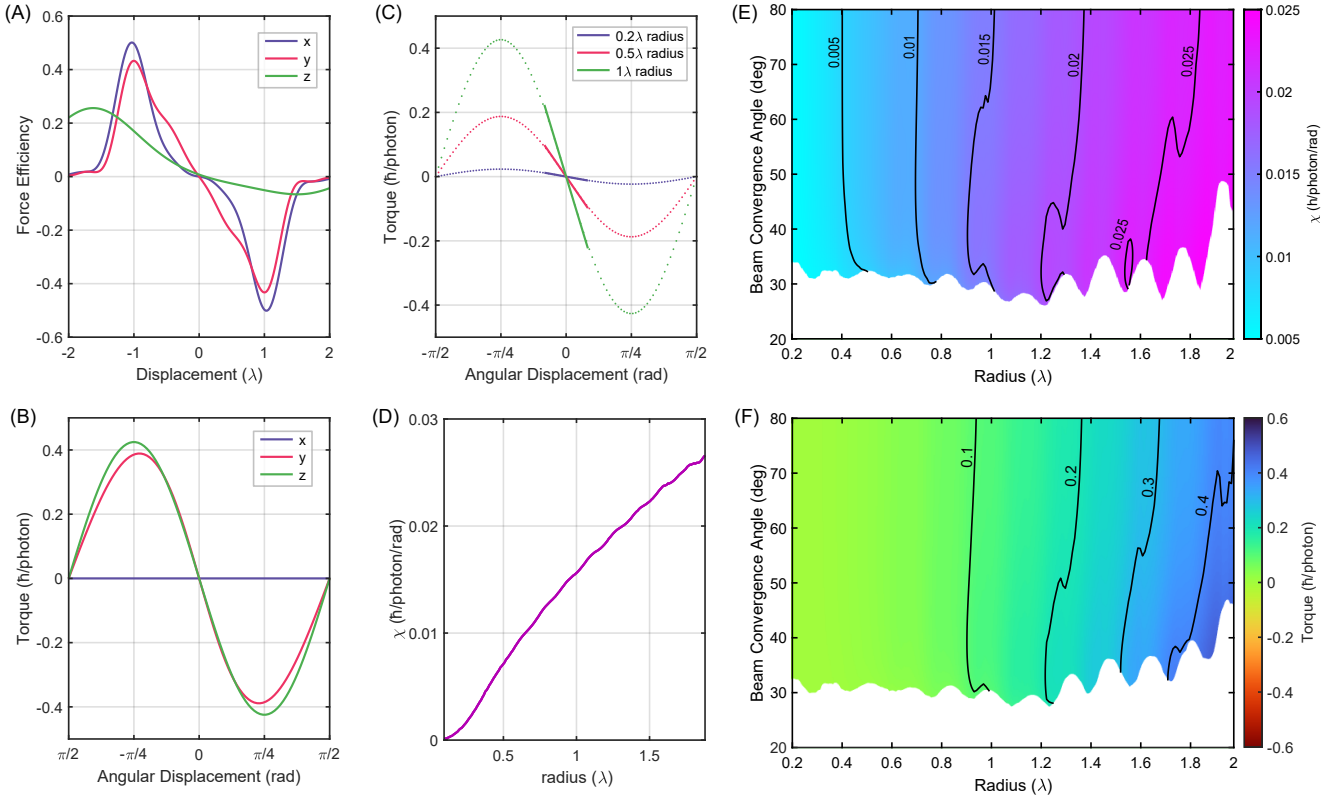


Figure 3. (A) The force profile for a 1λ radius probes. (B) The torque profile for a 1λ radius vaterite showing rotation about each axis. (C) The torque profile about z for three differently sized probes. (D) The calculated χ for a given radius using the torque profile method. (E) Heatmap of the angular trap stiffness relative to beam size and beam convergence angle for a vaterite probe. (F) A heatmap of the optical torque on a vaterite probe when illuminated in circularly polarised light. In both (E) and (F), only the conditions where a stable spatial trap occurs are plotted, with the probe positioned at its equilibrium position along the beam axis as calculated from the force profile.

be noted, however, that these results are specific to the canonical trapping configuration considered here and do not account for additional factors.

V. PARAMETERS INFLUENCING ANGULAR STIFFNESS AND ROTATIONAL DYNAMICS

While the preceding analysis has focussed on the optical forces and torques in a standard trapping configuration, a more complete description of the system requires consideration of additional physical and geometrical effects. In this section, we examine the role of hydrodynamic and inertial contributions to the probe’s motion, discuss the influence of variations in vaterite morphology, and explore how the presence of the measurement beam modifies the trapping dynamics. It is important to note that we do not address limitations associated with experimental detection, such as the accuracy of spin-basis torque measurements or the impact of optical misalignments, as these are beyond the scope of the present work.

A. The Helium-Neon Measurement Beam

In our experimental system, an ancillary measurement beam is introduced to probe the angular dynamics of the trapped particle. As described in Section II, this is a low-powered and weakly focussed circularly polarised 633 nm Helium-Neon laser. Owing to its low intensity and reduced numerical aperture, the measurement beam is treated as a passive probe of angular position that does not perturb the rotational dynamics of the probe. In this section, we investigate the validity and limitations of this assumption.

The circularly polarised measurement beam exerts a constant optical torque on the probe, which causes a shift in the equilibrium orientation of the probe in the direction of the applied torque. This displaces the probe from the zero-torque point of the trapping beam, corresponding to a reduction in the angular stiffness. However, a sufficiently large change in equilibrium orientation, $\Delta\phi_0$, can push the probe beyond the linear regime of the restoring torque, where stiffness estimates become less reliable. The measurement beam also affects the probe’s axial trapping, which varies the angular stiffness as opti-

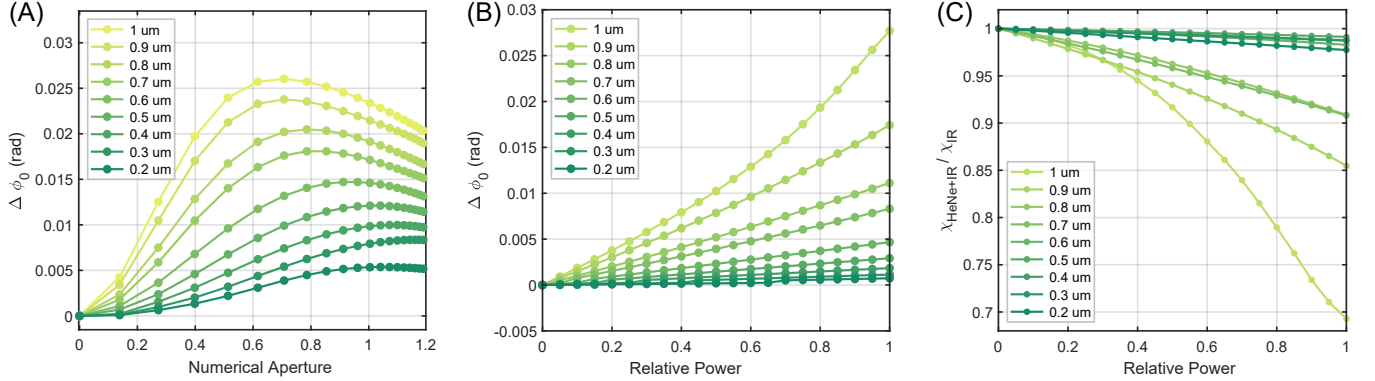


Figure 4. The influence of the measurement beam on the equilibrium orientation of the probe and its angular trap stiffness for several probe sizes. (A) The shift in equilibrium orientation is attributed to varying the numerical aperture of the measurement beam, which has a relative power of 0.1 of the trapping beam. (B) The shift in equilibrium and (C) relative change in angular trap stiffness, corresponds to the relative power of the measurement beam (NA 1.2).

cal torque is maximised near the beam focus. Hence, the combined influence of rotational and translational effects relative to the measurement beam's parameters must be properly understood when interpreting angular dynamics.

Fig. 4 examines the influence of the He-Ne beam's numerical aperture and its power relative to the trapping beam on the angular dynamics of the probe. Panel A shows the change in the equilibrium displacement as a function of its effective numerical aperture. The non-monotonic behaviour is specific to the rotational regime, as it is due to the coupling between the spin-angular momentum of the focussed beam and the inhomogeneous internal structure of the birefringent probe. Hence, the convergence angle that gives the maximum increase to stiffness is size-dependent.

Fig. 4B-C shows the influence of the second key beam parameter, the optical power, with respect to the shift in ϕ_0 and the relative change in angular stiffness. As expected, increased power results in a greater equilibrium shift and reduction in stiffness. Typically, the power of the measurement beam is maintained near 1 mW-10 mW, while the trapping beam is varied from 50 mW-300 mW. Consequently, the measurement beam contributed to an angular equilibrium shift on the order of a few milliradians, which maintains the rotational dynamics within the linear regime. Therefore, the measurement beam remains a passive probe with negligible impact on trap stability under conventional operating beam parameters. This shift in ϕ_0 only becomes significant for extremely sensitive rotational measurements, such as those in the rotational ballistic regime [24].

To explore the limits of this interaction, we consider the case where the relative power of the measurement beam is progressively increased beyond typical experimental conditions. At low beam convergence angles, increasing the He-Ne beam's power can destabilise the trap entirely, as the gradient forces from both beams become insufficient to counteract the scattering force from the

measurement beam. In such cases, no spatial trap is formed, and the probe escapes confinement. However, when a trap is formed, the constant torque from the circularly polarised beam can dominate the angular dynamics. As the torque from the measurement beam becomes comparable to or exceeds the restoring torque of the primary trap, the system enters a state of rotation instead of alignment. Hence, rotational dynamics are governed by the competition between alignment torque from the trapping beam and the rotation torque from the measurement beam.

Fig. 5 illustrates this behaviour, presenting a heat map of the relative power required to destabilise the system as a function of a probe size and measurement beam convergence angle. The line delineates the threshold between linear trap destabilisation and angular confinement failure. As expected, the axial trap fails to form at low numerical apertures, where the scattering force from the measurement beam dominates the total gradient force.

In addition to a destabilisation of angular trapping, there is also a relative beam power which causes the probe to depart from the translational regime. The departure from the linear regime causes the potential to become asymmetrical and no longer harmonic. Since the torque profile is a sinusoidal function, this is equivalent to asking: when does $\sin(2\phi) \approx 2\phi$, which can be defined as a sufficiently large shift in ϕ_0 . For example, setting $\phi_0 > \pi/12$ as the departure from the linear regime requires a relative power between 0.48 to 0.55 times the power required to destabilise the alignment. These powers are an order of magnitude larger than typical experiments.

The relative power required to prevent angular trapping or depart from the translational regime is inversely related to the probe size. It becomes difficult to induce rotation for smaller probes, which has significant consequences for rotational measurements of nano- and sub-micron particles. These particles have low scattering cross-sections, which can drastically reduce the signal-to-

noise in optical detection schemes. However, the power and convergence angle of the measurement beam can be optimised to enhance detection sensitivity without disrupting their expected dynamics. As shown in Fig. 5, angular trapping is maintained for smaller probes as the measurement beam power begins to surpass that of the trapping beam (provided axial trapping is achieved). This suggests that, contrary to conventional constraints, the measurement beam power can be increased to improve signal quality while preserving linear rotational dynamics.

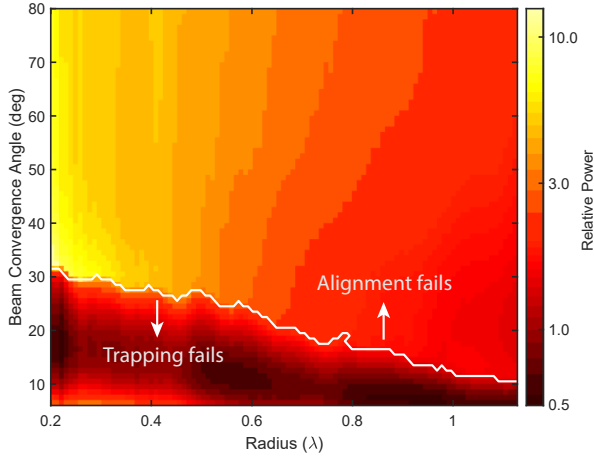


Figure 5. A heat map showing the He-Ne measurement beam power relative to the trapping IR beam that destroys the measurement. The dashed line separates the regions into cases where either the trap or alignment cannot be formed.

B. Spheroidal Vaterite Probes

The morphology of the vaterite probes varies between individual microspheres during synthesis, both in size and geometry. The probes have been observed to be slightly spheroidal, with the long axis aligned along their optic axis. To investigate how deviations from spherical geometry influence the angular trap stiffness, spheroidal vaterite probes were simulated with ellipticity introduced along the axis of rotational symmetry. The probe radius was defined along the fixed axes, and the aspect ratio was the length of the variable axis relative to this radius.

The angular trap stiffness increases with aspect ratio, as shown in Fig. 6. As the probe becomes elongated (aspect ratio > 1), it acquires shape-induced birefringence that aligns its long axis with the polarisation axis of the beam. This increases the angular trap stiffness as the shape and material birefringence contribute constructively. Conversely, when the probe becomes oblate (aspect ratio < 1), the shape birefringence opposes the

intrinsic material birefringence, resulting in a reduction in the angular stiffness.

The angular trap stiffness of smaller probes is more sensitive to changes in aspect ratio, as shown in Fig. 6,

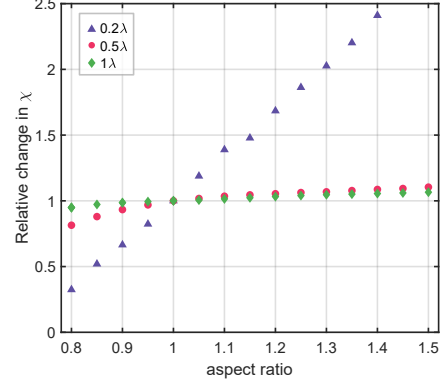


Figure 6. The influence of vaterite ellipticity on χ . The change in χ relative to a perfect spherical geometry (aspect ratio = 1) is shown

which displays the relative change in χ_ϕ . At smaller sizes, geometric variations have a greater impact because changes in surface curvature are more pronounced relative to the beam waist. As a result, the contribution of the shape-induced birefringence becomes more significant, leading to larger variations in stiffness.

In summary, deviations from spherical geometry introduce shape-induced birefringence that modifies the angular trap stiffness. This effect is size-dependent, with smaller probes exhibiting greater sensitivity to changes in aspect ratio due to enhanced curvature effects relative to the beam waist.

C. Hydrodynamic and Inertial contributions

The theoretical expressions used in stochastic analysis techniques are derived from the equation of motion (Eq. 5), in which inertial and hydrodynamic terms are typically neglected. While this is a valid approximation for most optical trapping experiments, these effects become increasingly relevant at higher frequencies and can introduce systematic errors if omitted. In the translational case, Berg-Sørensen and Flyvbjerg [15] argued that hydrodynamic corrections should always be included when fitting the position power spectrum when precision is important. It is therefore necessary to reassess the relative contributions of these effects in the rotational regime.

The full power spectrum model that considers these effects is given by:

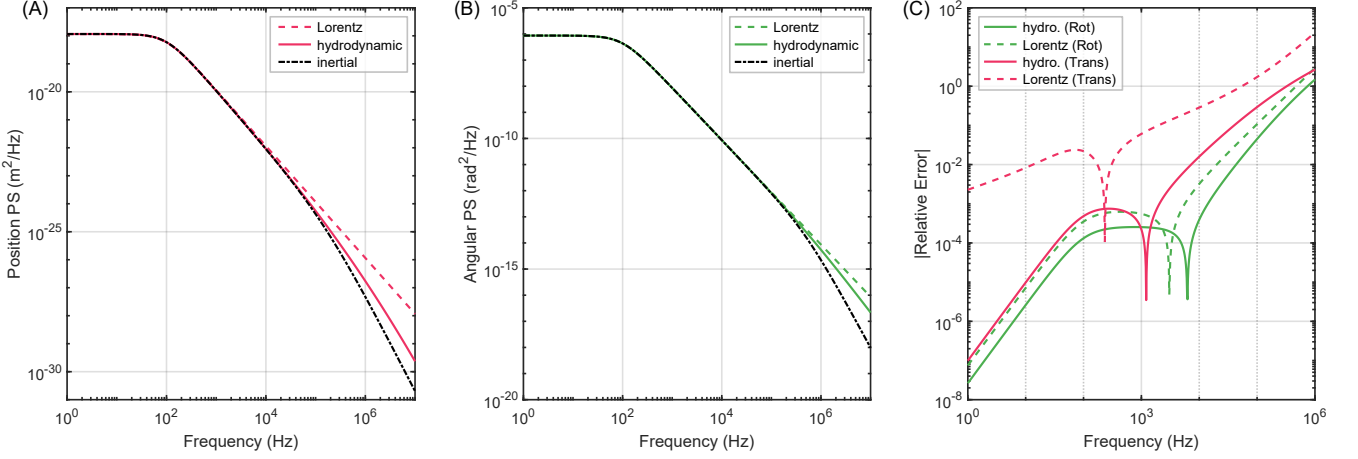


Figure 7. Position (A) and Angular Position (B) power spectra as expected following Lorentz theory (dashed lines), hydrodynamically-corrected theory (solid line), and the inertia-corrected theory (dot-dash black line). (C) shows the relative difference between the Lorentz and hydrodynamic theories to the inertia-corrected model. This is for a 1λ radius probe in a trap with a corner frequency of $f_c = 100$ Hz for both rotational and translational modes.

$$S(f) = \frac{D}{2\pi^2} \frac{\text{Re}(\gamma(f)/\gamma_0)}{(f_c - f^2/f_i + f \text{Im}(\gamma(f)/\gamma_0))^2 + (f \text{Re}(\gamma(f)/\gamma_0))^2}, \quad (27)$$

where f_i is the characteristic rate associated with the inertia dissipation, and $\gamma(f)$ is the frequency-dependent drag coefficient that accounts for hydrodynamic effects. This expression (Eq. 27) is valid for both translational and rotational motion in one dimension, assuming appropriate substitutions as outlined in Table 1 of Watson *et al.* [24]. The frequency-dependent drag coefficients for rotational and translational motion are given by

$$\gamma_r(f) = \gamma_{0,r} \left(1 - \frac{2i}{3} \frac{f/f_v}{1 - (1-i)\sqrt{f/f_v}} \right), \quad (28)$$

$$\gamma_t(f) = \gamma_{0,t} \left(1 + (1-i)\sqrt{f/f_v} - \frac{2i}{9} (f/f_v) \right), \quad (29)$$

where f_v is the characteristic frequency associated with the fluid relaxation. This model accurately captures the underlying dynamics of a probe in a viscous fluid across all experimentally accessible measurement rates. The inertial contribution can be neglected when $f \ll f_i$, as the term f^2/f_i becomes negligible. Similarly, the hydrodynamic modifications can be neglected when $f \ll f_v$, in which case the drag coefficient $\gamma(f)$ reduces to the standard Stokes form, γ_0 . However, the magnitude of f_v (on the order of 10^5 Hz for both regimes) is not a useful indicator for deciding whether the hydrodynamic contributions can be neglected—particularly in the translational regime. Unlike f_i and f_c , which introduce well-defined corner frequencies into the power spectrum, the hydrodynamic contribution alters the spectrum over a much broader frequency range due to the functional form of $\gamma(f)$.

In this section, we compare analytical power spectra generated by three models: the Lorentzian model, the hydrodynamically corrected theory, and the inertia-corrected theory, which incorporates both inertial and hydrodynamic effects. Since $f_i > f_v$, the hydrodynamic contribution must be included whenever inertial effects are considered. These models are shown in Fig. 7A-B for the translational and rotational regimes, respectively. The inertia-corrected model provides the most accurate description of the probe's dynamics and is therefore the reference for comparison. The relative error between the Lorentzian and the hydrodynamically-corrected models, with respect to the inertia-corrected model, is shown in Fig. 7C for both translational and rotational motion. This figure provides a practical guide for determining which model is required to achieve a desired level of precision.

Regardless of the desired precision, the hydrodynamic and inertial contributions in the rotational are significantly smaller than their translational counterparts across most frequencies. In the rotational case, the combined contribution remains below 0.1% for frequencies up to 5.5 kHz. By contrast, in the translational regime, the hydrodynamic contributions exceed 1% at only 13 Hz, supporting the argument that it should always be included when fitting translational power spectra. This stark difference highlights the reduced sensitivity of rotational motion to fluid-mediated effects, which makes the simplified models—such as the Lorentzian—more broadly applicable in rotational optical trapping.

It is important to note that the relative errors presented here correspond to a specific probe size and corner

frequency. These thresholds shift with different experimental parameters. For example, increasing the probe size decreases both f_v and f_i , thereby lowering the frequency range over which hydrodynamic and inertial effects become significant. If a simplified model is preferred for fitting, we recommend first recalculating the relative error curves (as shown in Fig. 7C) using the expected system parameters to ensure the model remains valid within the desired precision.

Our analysis reveals that these effects play a comparatively minor role in the rotational case. This difference arises from the distinct scaling of rotational drag and inertia, which reduces their impact on the angular power spectrum within the frequency range typically probed in experiments. Since most ROTs measurements are performed at a rate on the order of 10^4 Hz. Once the data is truncated to the Nyquist frequency, the hydrodynamic and inertial contributions become small enough to be ignored. Conversely, translational measurements performed at a similar rate can ignore the inertial contributions but should still incorporate the hydrodynamic effect term.

VI. DISCUSSION

The calibration of rotational optical tweezers requires independent consideration of angular dynamics. Rotational and translational degrees of freedom appear analogous, due to the linearised model of their dynamics near equilibrium. This is demonstrated by the excellent agreement in determining angular stiffness from passive calibration techniques. Beyond this regime, the physical interactions governing rotational and translational motion differ notably. This study investigates important factors that determine angular trap stiffness, including probe geometry, hydrodynamic effects, and contributions from the ancillary measurement beam used in angular detection.

Optical tweezers are an attractive tool for investigating the mechanical properties of microscopic systems, owing to their ability to confine probes with high spatial precision. This capability is particularly advantageous for confined environments, such as microstructures and intracellular compartments. The use of rotational geometry and nanoparticles as probes further enhances the

versatility of trapping experiments.

The geometry and morphology of the probe have unique effects on the interaction with the optical potential and its underlying dynamics. The dynamics of spheroidal probes depend on the combination of shape-induced and material birefringence, and are amplified for smaller probes. Conversely, hydrodynamic and inertial effects are reduced, allowing them to be ignored in models of rotational dynamics at typical detection sensitivities.

The parameters of both the trapping and measurement beams can influence the dynamics of the probe and the quality of the measurement. We demonstrated that the influence of the ancillary beam on the angular dynamics is minimal even when the beam parameters surpass the conventional limitations and decreases with probe size. This is particularly important for nanoparticles, which produce weak signals in optical detection schemes and make measurements of their dynamics more challenging. Unlike in the translational case, where increasing optical power alters the trapping dynamics, increasing the power of an ancillary beam in rotational optical tweezers enhances detection sensitivity without compromising the expected angular dynamics.

In summary, these findings highlight the importance of treating translational and rotational dynamics as independent features of optical tweezers. Although their behaviour may initially appear analogous due to the linearised description of their dynamics near equilibrium, variations in experimental parameters yield profoundly different outcomes. Our work demonstrates the need for tailored approaches for calibrating and quantifying rotational optical tweezers independently from standard optical tweezers. This will lead to more accurate and targeted use of rotational optical tweezers in studies of complex microsystems, particularly towards nano-scale environments.

VII. ACKNOWLEDGEMENTS

This work was funded by the Australian Research Council Centre of Excellence for Quantum Biotechnology (CE230100021) and Australian Research Council Discovery Project (DP230100675). We would like to thank Timo Nieminen and Giovanni Volpe for illuminating discussions and ideas that helped enhance this work.

[1] A. Ashkin, J. M. Dziedzic, J. E. Bjorkholm, and S. Chu, *Optics Letters* **11**, 288 (1986).

[2] P. H. Jones, O. M. Maragò, and G. Volpe, *Optical tweezers: Principles and applications* (Cambridge University Press, Cambridge, 2015).

[3] G. Volpe, O. M. Maragò, H. Rubinsztein-Dunlop, G. Pesce, A. B. Stilgoe, G. Volpe, G. Tkachenko, V. G. Truong, S. N. Chormaic, F. Kalantarifard, P. Elahi, M. Käll, A. Callegari, M. I. Marqués, A. A. R. Neves, W. L. Moreira, A. Fontes, C. L. Cesar, R. Saija, A. Saidi, P. Beck, J. S. Eismann, P. Banzer, T. F. D. Fernandes, F. Pedaci, W. P. Bowen, R. Vaippully, M. Lokesh, B. Roy, G. Thalhammer-Thurner, M. Ritsch-Marte, L. P. García, A. V. Arzola, I. P. Castillo, A. Argun, T. M. Muenker, B. E. Vos, T. Betz, I. Cristiani, P. Minzioni, P. J. Reece, F. Wang, D. McGloin, J. C. Ndukaife, R. Quidant, R. P. Roberts, C. Laplane, T. Volz, R. Gordon, D. Hanstorp, J. T. Marmolejo, G. D. Bruce, K. Dholakia, T. Li,

O. Brzobohatý, S. H. Simpson, P. Zemánek, F. Ritort, Y. Roichman, V. Bobkova, R. Wittkowski, C. Denz, G. V. P. Kumar, A. Foti, M. G. Donato, P. G. Gucciardi, L. Gardini, G. Bianchi, A. V. Kashchuk, M. Capitanio, L. Paterson, P. H. Jones, K. Berg-Sørensen, Y. F. Barrooji, L. B. Oddershede, P. Pouladian, D. Preece, C. B. Adiels, A. C. De Luca, A. Magazzù, D. Bronte Ciriza, M. A. Iatì, and G. A. Swartzlander, *Journal of Physics: Photonics* **5**, 022501 (2023), publisher: IOP Publishing.

[4] K. Norregaard, R. Metzler, C. M. Ritter, K. Berg-Sørensen, and L. B. Oddershede, *Chemical Reviews* **117**, 4342 (2017).

[5] W. J. Weigand, A. Messmore, J. Tu, A. Morales-Sanz, D. L. Blair, D. D. Dehenn, J. S. Urbach, and R. M. Robertson-Anderson, *PLOS ONE* **12**, e0176732 (2017).

[6] M. L. Watson, D. L. Brown, A. B. Stilgoe, J. L. Stow, and H. Rubinsztein-Dunlop, *Optica* **9**, 1066 (2022).

[7] B. E. Vos, T. M. Muenker, and T. Betz, *Current Opinion in Cell Biology* **88**, 102374 (2024).

[8] S. M. Block, L. S. B. Goldstein, and B. J. Schnapp, *Nature* **348**, 348 (1990).

[9] W. Singer, M. Frick, T. Haller, S. Bernet, M. Ritsch-Marte, and P. Dietl, *Biophys J* **84**, 1344 (2003).

[10] E. Fällman, S. Schedin, J. Jass, M. Andersson, B. E. Uhlin, and O. Axner, *Biosensors and Bioelectronics* **19**, 1429 (2004).

[11] J. Inman, S. Forth, and M. D. Wang, *Optics Letters* **35**, 2949 (2010).

[12] F. Català-Castro, E. Schäffer, and M. Krieg, *Journal of Cell Science* **135**, 10.1242/jcs.259355 (2022).

[13] S. Chakraborty, G. Nalupurackal, S. Roy, M. Lokesh, J. Goswami, M. Gunaseelan, and B. Roy, *Optics Express* **31**, 42230 (2023).

[14] Y. Hong, F. Ye, J. Qian, X. Gao, J. T. Inman, and M. D. Wang, *Biophysical Journal* **123**, 3080 (2024).

[15] K. Berg-Sørensen and H. Flyvbjerg, *Review of Scientific Instruments* **75**, 594 (2004), publisher: AIP Publishing.

[16] J. Gieseler, J. R. Gomez-Solano, A. Magazzù, I. Pérez Castillo, L. Pérez García, M. Gironella-Torrent, X. Viader-Godoy, F. Ritort, G. Pesce, A. V. Arzola, K. Volke-Sepúlveda, and G. Volpe, *Advances in Optics and Photonics* **13**, 74 (2021).

[17] S. Mirzaei-Ghormish, *Physical Review A* **111**, 10.1103/PhysRevA.111.013514 (2025).

[18] M. E. J. Friese, T. A. Nieminen, N. R. Heckenberg, and H. Rubinsztein-Dunlop, *Nature* **394**, 348 (1998).

[19] A. I. Bishop, T. A. Nieminen, N. R. Heckenberg, and H. Rubinsztein-Dunlop, *Physical Review Letters* **92**, 198104 (2004).

[20] Y. Arita, J. M. Richards, M. Mazilu, G. C. Spalding, S. E. Skelton Spesvtseva, D. Craig, and K. Dholakia, *ACS Nano* **10**, 11505 (2016).

[21] B. Roy, S. K. Bera, and A. Banerjee, *Optics Letters* **39**, 3316 (2014).

[22] J. Ma, C. Tan, and M. D. Wang, *Single-Molecule Angular Optical Trapping for Studying Transcription Under Torsion*, edited by C. Lavelle and J. M. Walker, Molecular Motors: Methods and Protocols, Vol. 1805 (Springer New York, New York, NY, 2018).

[23] J. S. Bennett, L. J. Gibson, R. M. Kelly, E. Brousse, B. Baudisch, D. Preece, T. A. Nieminen, T. Nicholson, N. R. Heckenberg, and H. Rubinsztein-Dunlop, *Scientific Reports* **3**, 1759 (2013).

[24] M. L. Watson, A. B. Stilgoe, I. A. Favre-Bulle, and H. Rubinsztein-Dunlop, *Optica* **12**, 246 (2025).

[25] S. Zhang, L. J. Gibson, A. B. Stilgoe, I. A. Favre-Bulle, T. A. Nieminen, and H. Rubinsztein-Dunlop, *Optica* **4**, 1103 (2017).

[26] F. Pedaci, Z. Huang, M. Van Oene, and N. H. Dekker, *Optics Express* **20**, 3787 (2012).

[27] J. Leach, H. Mushfique, S. Keen, R. Di Leonardo, G. Ruocco, J. M. Cooper, and M. J. Padgett, *Physical Review E* **79**, 026301 (2009).

[28] L. J. Gibson, S. Zhang, A. B. Stilgoe, T. A. Nieminen, and H. Rubinsztein-Dunlop, *Physical Review E* **99**, 043304 (2019).

[29] K. Makuch, R. Hołyst, T. Kalwarczyk, P. Garstecki, and J. F. Brady, *Soft Matter* **16**, 114 (2020).

[30] J. Michalski, T. Kalwarczyk, K. Kwapiszewska, J. Enderlein, A. Poniewierski, A. Karpińska, K. Kucharska, and R. Hołyst, *Soft Matter* **20**, 5810 (2024), publisher: Royal Society of Chemistry.

[31] R. Vogel, M. Persson, C. Feng, S. J. Parkin, T. A. Nieminen, B. Wood, N. R. Heckenberg, and H. Rubinsztein-Dunlop, *Langmuir* **25**, 11672 (2009).

[32] M. Lokesh, R. Vaippully, V. P. Bhallamudi, A. Prabhakar, and B. Roy, *Journal of Physics Communications* **5**, 115016 (2021).

[33] S. Roy, R. Vaippully, M. Lokesh, G. Nalupurackal, P. Edwina, S. Bajpai, and B. Roy, *Frontiers in Physics* **10**, 10.3389/fphy.2022.1099958 (2023).

[34] T. A. Nieminen, V. L. Y. Loke, A. B. Stilgoe, G. Knöner, A. M. Brańczyk, N. R. Heckenberg, and H. Rubinsztein-Dunlop, *Journal of Optics A: Pure and Applied Optics* **9**, S196 (2007).

[35] T. A. Nieminen, V. L. Y. Loke, A. B. Stilgoe, N. R. Heckenberg, and H. Rubinsztein-Dunlop, *Journal of Modern Optics* **58**, 528 (2011).

[36] J. H. Crichton and P. L. Marston, *Electronic journal of differential equations Conf.* **04**, 37 (2000).

[37] V. L. Y. Loke, T. A. Nieminen, N. R. Heckenberg, and H. Rubinsztein-Dunlop, *Journal of Quantitative Spectroscopy and Radiative Transfer* **110**, 1460 (2009).

[38] D. C. Champeney, *A handbook of Fourier theorems* (Cambridge University Press, 1987).

[39] L. Pérez García, J. Donlucas Pérez, G. Volpe, A. V. Arzola, and G. Volpe, *Nature Communications* **9**, 5166 (2018).

[40] A. B. Stilgoe, D. J. Armstrong, and H. Rubinsztein-Dunlop, *Micromachines* **12**, 570 (2021).

[41] A. B. Stilgoe, T. A. Nieminen, G. Knöner, N. R. Heckenberg, and H. Rubinsztein-Dunlop, *Optics Express* **16**, 15039 (2008).